



Contents lists available at ScienceDirect



An augmented-Lagrangian method for the phase-field approach for pressurized fractures



M.F. Wheeler^a, T. Wick^{a,*}, W. Wollner^b

^aThe Institute for Computational Engineering and Sciences, The University of Texas at Austin, Austin, TX 78712, USA

^bDepartment of Mathematics, University of Hamburg, 20146 Hamburg, Germany

ARTICLE INFO

Article history:

Received 19 August 2013

Received in revised form 27 November 2013

Accepted 16 December 2013

Available online 24 December 2013

MSC:

65N30

65M60

74F99

Keywords:

Finite elements

Phase-field

Variational fracture

Augmented Lagrangian

Iterative solution

ABSTRACT

In the modeling of pressurized fractures using phase-field approaches, the irreversibility of crack growth is enforced through an inequality constraint on the temporal derivative of the phase-field function. In comparison to the classical case in elasticity, the presence of the pressure requires the additional constraint and makes the problem much harder to analyze. After temporal discretization, this induces a minimization problem in each time step over a solution dependent admissible set. To avoid solving the resulting variational inequality corresponding to the first order necessary conditions, a penalization approach is used, commonly, to remove the inequality constraint. It is well-known that for large penalty parameters the algorithm suffers from numerical instabilities in the solution process. Consequently, to avoid such a drawback, we propose an augmented Lagrangian algorithm for the discrete in time and continuous in space phase-field problems. The final set of equations is solved in a decoupled fashion. The proposed method is substantiated with several benchmark and prototype tests in two and three dimensions.

© 2013 Elsevier B.V. All rights reserved.

1. Introduction

Presently, crack propagation in elastic and porous media is one of the major research topics in energy and environmental engineering. Consequently, many models and numerical techniques have been investigated so far. Specifically, Griffith's model [1] for quasi-static fracture evolution has been successfully applied. Here, the crack propagates if the rate of elastic energy decrease per unit surface area of the increment step is equal to the quasi-static critical energy release rate G_c . The crack does not move if the elastic energy release rate is less than G_c . On the contrary, it is unstable if G_c exceeds the critical rate. Griffith found that G_c is related to the crack surface energy increase. The solution of crack representation and propagation requires special techniques for their numerical treatment. In recent years, different approaches have been proposed such as the extended finite element method by Moes et al. [2] based on the partition of unity method of Babuska and Belenk [3] in which the displacement field is enriched with discontinuities. In addition, fixed-mesh approaches such as phase-field techniques have gained increased interest by studies from Francfort and Marigo [4], Bourdin et al. [5,6], Miehe et al. [7,8], Borden et al. [9], Hofacker and Miehe [10]. Instead of modeling the discontinuities explicitly (like in the extended finite element method), the lower-dimensional crack surface is approximated by a phase-field function. This introduces a diffusive

* Corresponding author. Tel.: +1 512 232 7763.

E-mail addresses: mfw@ices.utexas.edu (M.F. Wheeler), twick@ices.utexas.edu (T. Wick), winnifried.wollner@uni-hamburg.de (W. Wollner).

transition zone (brittle zone or mushy-zone are also common expressions depending on the discipline) between the broken and the unbroken material; see Fig. 1.

The major advantages of using phase-field modeling for crack propagation are fourfold. First, it is a fixed-mesh approach in which remeshing is avoided. Second, the model is purely based on energy minimization and therefore, crack nucleation, propagation and the path are automatically determined (avoiding calculation of additional components such as stress intensity factors). Third, multiple joining and branching of cracks do not require any additional techniques. Consequently, phase-field modeling allows simple handling of large and complex fracture networks. Fourth, crack growth in heterogeneous media does not require any modification in the framework. Quantities of interest such as the crack opening displacement (the aperture) can be recovered with the help of the phase-field function. From the application point of view, we are specifically interested in pressurized fractures and their propagation, which are of particular interest in dam constructions, subsurface modeling, blood flow with damaged tissue, and oil recovery processes. In recent years, several methods for pressurized fracture and crack propagation have been proposed. These include an implicit moving mesh algorithms of Lecampion and Detournay [12]; moving-mesh approach with local grid refinement by Schrefler et al. [13]; a special zero-thickness finite element approach by Carrier and Granet [14]; the partition of unity and extended finite element approaches by Irzal et al. [15]; and finally, boundary element approaches by Ganis et al. [16] and Castonguay et al. [17]. To the best of our knowledge, the previously mentioned phase-field approach was first applied to pressurized cracks by Bourdin et al. [18], and a rigorous model investigation was first undertaken by Mikelić et al. [19,11] (See Fig. 2).

In this paper, we extend the previous studies [19,11]. Namely, the penalization of the irreversibility condition for crack growth is modified. It is well-known from Lootsma [20] and Murray [21] that simple penalization leads to numerical instabilities due to ill-conditioning of the constraint Hessian. Consequently, another (but computational costly) method is proposed by Mikelić et al. [11]. We circumvent these drawbacks in adapting a robust method from optimization: the augmented Lagrangian method dating back to Hestenes [22], Powell [23] and proposed by Fortin and Glowinski [24], Glowinski and Tallec [25] for use in discretized differential equations. In particular, we consider the augmented Lagrangian in a function space setting similar to Ito and Kunisch [26, Chapter 4].

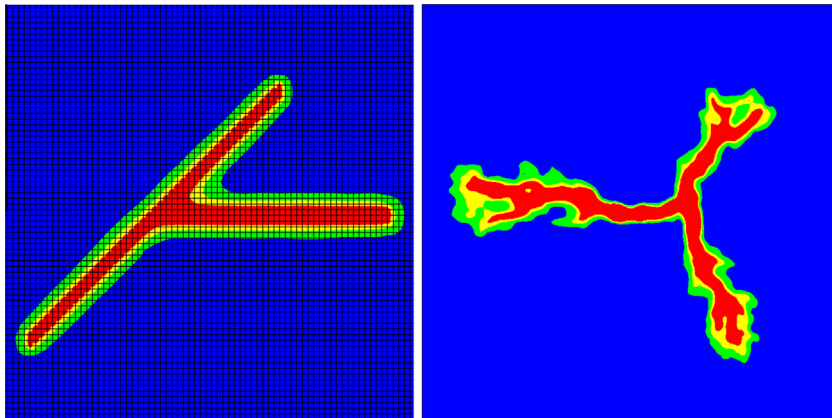


Fig. 1. Explication of the fixed-grid finite element phase-field approach: a (lower-dimensional) crack is approximated with the help of a phase-field function as shown in the left figure. The phase-field is an indicator function with values 0 in the crack (here in red) and 1 in the unbroken zone (here in blue). The mushy-zone provides a smooth interpolation between 0 and 1 indicated in yellow and green. On the right side, the major advantages for the phase-field approach are shown: joining, branching and nonplanar crack growth in possibly heterogeneous media (figure taken from [11]). (For interpretation of the references to colour in this figure caption, the reader is referred to the web version of this article.)

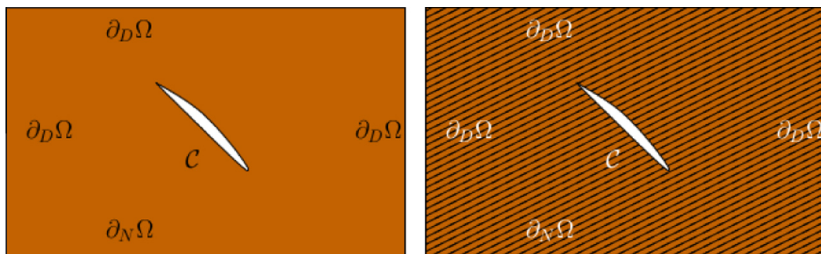


Fig. 2. Prototype configurations of the setting. The difference between Bourdin's approach [18] (left) and our approach (right) is that he works in an elastic medium whereas we work in a poroelastic setting.

Here, the numerical discretization is based on the incremental formulation [11]. In particular, a Galerkin finite element scheme is used for spatial discretization. The solution algorithm is based on a decoupling of the equations, which allows for easy extension to sophisticated solvers for each of the subproblems. This is in particular interesting for large-field 3d simulations. Since the augmented Lagrangian method is based on an iteration itself, we perform several subiterations until the change in displacements is sufficiently small. The nonlinear phase-field equation is solved with Newton's method whereas the elasticity problem is linear.

The paper is organized as follows: In Section 2, we recall the energy functionals defined on the continuous level. In Section 3, the augmented Lagrangian is derived with respect to the energy functional. Next, in Section 4, the corresponding Euler–Lagrange equations and their discretization are discussed. Moreover, our solution algorithm is described. The final Section 5 presents four different examples for pressurized cracks in two and three dimensions. We propose simple configurations that might allow comparisons with other methods for crack propagation and we provide a deeper understanding of the capabilities of our method by studying several numerical aspects.

2. The energy functional

Let $\Omega \in \mathbb{R}^d$, $d = 2, 3$ be a given domain. We assume that the crack \mathcal{C} is contained compactly in Ω , i.e., it does not reach the boundary. Let us denote by $(\cdot, \cdot)_A$, $\|\cdot\|_A$ the usual L^2 -inner product and norm on A . If $A = \Omega$ we skip the subscript for better readability.

Following Griffith's criterion, we suppose that the crack propagation occurs when the elastic energy restitution rate reaches its critical value G_c . If τ is the traction force applied at the part of the boundary $\partial_N \Omega$, we then associate to the crack \mathcal{C} the following total energy [11, 19].

$$E(\eta, \mathcal{C}) = \frac{1}{2} (\mathcal{G}e(\eta), e(\eta))_{\Omega \setminus \mathcal{C}} - \langle \tau, \eta \rangle_{\partial_N \Omega} - (\alpha - 1)(p_B, \operatorname{div} \eta)_{\Omega \setminus \mathcal{C}} + (\nabla p_B, \eta)_{\Omega \setminus \mathcal{C}} + G_c \mathcal{H}^{d-1}(\mathcal{C}), \quad (1)$$

where η denotes the vector-values displacement field, p_B is the poroelastic medium pressure, $\alpha \in [0, 1]$ is the Biot coefficient, \mathcal{H}^{d-1} is the $d - 1$ -dimensional Hausdorff measure, and \mathcal{G} the rank-4 Gassman tensor. Later, we use the law

$$\mathcal{G}e(\eta) = \sigma(\eta) = 2\mu_s e(\eta) + \lambda_s \operatorname{tr} e(\eta) I,$$

where μ_s and λ_s denote the Lamé coefficients, $e(\eta) = \frac{1}{2}(\nabla \eta + \nabla \eta^T)$, and I the identity in d -dimensions.

This energy functional is then minimized with respect to the kinematically admissible displacements η and any crack set satisfying a crack growth condition. The computational modeling of this minimization problem should treat complex crack topologies and requires approximation of the crack location and of its length. This can be overcome by regularizing the sharp crack surface topology in the solid by diffusive crack zones described by a scalar auxiliary variable. This variable is a phase-field that interpolates between the unbroken and the broken states of the material. As previously stated above for the purely solid mechanics problem variational methods were introduced by Bourdin et al. [5,6].

We introduce the time-dependent crack phase-field φ , defined on $\Omega \times (0, T)$. The regularized crack functional reads

$$\Gamma_\varepsilon(\varphi) = \frac{1}{2\varepsilon} \|1 - \varphi\|^2 + \frac{\varepsilon}{2} \|\nabla \varphi\|^2 = \int_{\Omega} \gamma(\varphi, \nabla \varphi) dx, \quad (2)$$

where γ is the crack surface density per unit volume. This regularization of $\mathcal{H}^{d-1}(\mathcal{C})$, in the sense of the Γ -limit when $\varepsilon \rightarrow 0$, was used in [5,6].

Our modeling part is based on the fact that the crack can only grow, which is represented by the irreversibility constraint:

$$\partial_t \varphi \leqslant 0. \quad (3)$$

In the following, we replace the energy (1) by a global constitutive dissipation functional for a rate independent fracture process [7,18,19]. We obtain then

$$\begin{aligned} E_\varepsilon(\eta, \varphi) &= \frac{1}{2} (((1 - \kappa)\varphi^2 + \kappa)\mathcal{G}e(\eta), e(\eta)) - \langle \tau, \eta \rangle_{\partial_N \Omega} - (\alpha - 1)(\varphi^2 p_B, \operatorname{div} \eta) + (\varphi^2 \nabla p_B, \eta) \\ &\quad + G_c \left(\frac{1}{2\varepsilon} \|1 - \varphi\|^2 + \frac{\varepsilon}{2} \|\nabla \varphi\|^2 \right), \end{aligned} \quad (4)$$

where κ is a positive regularization parameter for elastic energy, with $\kappa \ll \varepsilon$. We notice the meaning of the different terms in (4). The first term denotes the elastic bulk energy and the final term characterizes the surface energy of the crack. These two terms are already well-known from the pure elastic case. The middle line is novel and is a contribution from the pressure in the fracture [11, 19].

In the following, we work in a quasi-static formulation and velocity changes are assumed to be negligible. Consequently, we replace the time derivative $\partial_t \varphi$ by a backward difference quotient

$$\partial_t \varphi \approx \partial_k \varphi = \frac{\varphi - \varphi^{n-1}}{k},$$

where $k > 0$ denotes the time step parameter and $\varphi := \varphi^n$ the present solution and φ^{n-1} the solution to the previous time step. Discretization in time at this stage leads to an incremental formulation. With this we have

$$\varphi \leq \varphi^{n-1}$$

which means that the crack should not shrink in each incremental step. Remember (see Fig. 1) that the crack region is characterized by $\varphi = 0$ and the non-fractured zone by $\varphi = 1$.

3. The augmented Lagrangian method

The major novelty in this study is to impose the irreversibility constraint (3). To pose it in a minimization setting in function spaces, let us denote $V := H_0^1(\Omega)$ and $W := H^1(\Omega)$. Then given a previous time step solution $(\eta^{n-1}, \varphi^{n-1}) \in V \times W$ we seek $(\eta^n, \varphi^n) \in V \times W$ satisfying

$$\begin{aligned} \min \quad & E_\epsilon(\eta^n, \varphi^n) \\ \text{s.t.} \quad & \varphi^n \in K(\varphi^{n-1}) := \{\varphi \mid 0 \leq \varphi^n \leq \varphi^{n-1} \leq 1\}, \end{aligned} \quad (5)$$

or equivalently

$$\min E_\epsilon(\eta^n, \varphi^n) + I_{K(\varphi^{n-1})}(\varphi^n), \quad (6)$$

with the indicator function I_S of an arbitrary set S given by

$$I_S = \begin{cases} 0 & \text{on } S, \\ +\infty & \text{otherwise.} \end{cases}$$

Since $K(\varphi^{n-1})$ is closed, convex, and non-empty $I_{K(\varphi^{n-1})} : L^2(\Omega) \rightarrow \mathbb{R} \cup \{\pm\infty\}$ is proper, convex, and lower semi-continuous.

A rather simple penalization technique, to eliminate the extended real valued function $I_{K(\varphi^{n-1})}$, is used in [19], where the approximation

$$I_{K(\varphi^{n-1})} \approx \gamma((\varphi - \varphi^{n-1})^+)^2,$$

for $\gamma \rightarrow \infty$ is considered. Here, we denote by the superscript $+$ the positive part of a function, i.e.,

$$f^+ = \max(0, f).$$

However, it is well-known that this leads to numerical instabilities in the solution process. Another penalization of theoretical importance is employed in [11]. This one has however the drawback that it is very difficult to implement and rather expensive since second order derivatives need to be evaluated. Consequently, we aim for a simple but powerful strategy, which is provided by the augmented Lagrangian penalization. It is well-known in approaches as constraint optimization and in solving variational inequalities.

To avoid the non-differentiability of $I_{K(\varphi^{n-1})}$, while not increasing $\gamma \rightarrow \infty$, we introduce its Moreau–Yosida approximation, see, e.g., [26, Section 4.4]. To do so, let $\gamma \in \mathbb{R}_{>0}$, $\varphi, \lambda \in L^2(\Omega)$ be given. We define

$$M_\gamma(\varphi, \lambda) = \inf_{\psi \in L^2(\Omega)} (I_{K(\varphi^{n-1})}(\varphi - \psi) + (\lambda, \psi) + \frac{\gamma}{2} \|\psi\|^2). \quad (7)$$

M_γ is, again, convex and Frechét differentiable with respect to φ , see, e.g., [26, Theorem 4.39]. In the present case, the unique minimizer φ_γ on the right of the definition of $M_\gamma(\varphi, \lambda)$ in (7) is given by

$$\begin{aligned} \varphi_\gamma &= \min \left(\varphi, \max \left(\varphi - \varphi^{n-1}, -\frac{1}{\gamma} \lambda \right) \right) = \min \left(\varphi, (\varphi - \varphi^{n-1}) + \left((\varphi^{n-1} - \varphi) - \frac{1}{\gamma} \lambda \right)^+ \right) \\ &= \min \left(\varphi, (\varphi - \varphi^{n-1}) + \frac{1}{\gamma} \lambda + \left((\varphi^{n-1} - \varphi) - \frac{1}{\gamma} \lambda \right)^+ - \frac{1}{\gamma} \lambda \right) = \min \left(\varphi, \frac{1}{\gamma} ((\lambda + \gamma(\varphi - \varphi^{n-1}))^+ - \lambda) \right) \\ &= \frac{1}{\gamma} \min(\gamma\varphi, (\lambda + \gamma(\varphi - \varphi^{n-1}))^+ - \lambda) = \frac{1}{\gamma} (\min(\lambda + \gamma\varphi, (\lambda + \gamma(\varphi - \varphi^{n-1}))^+) - \lambda). \end{aligned}$$

Hence

$$\begin{aligned} M_\gamma(\varphi, \lambda) &= I_{K(\varphi^{n-1})}(\varphi - \varphi_\gamma) + (\lambda, \varphi_\gamma) + \frac{\gamma}{2} \|\varphi_\gamma\|^2 = (\lambda, \varphi_\gamma) + \frac{\gamma}{2} \|\varphi_\gamma\|^2 \\ &= \left(\lambda + \frac{1}{2} (\min(\lambda + \gamma\varphi, (\lambda + \gamma(\varphi - \varphi^{n-1}))^+) - \lambda), \varphi_\gamma \right) = \frac{1}{2\gamma} (\lambda + \min(\lambda + \gamma\varphi, (\lambda + \gamma(\varphi - \varphi^{n-1}))^+), \gamma\varphi_\gamma) \\ &= \frac{1}{2\gamma} \|\min(\lambda + \gamma\varphi, (\lambda + \gamma(\varphi - \varphi^{n-1}))^+)\|^2 - \frac{1}{2\gamma} \|\lambda\|^2. \end{aligned}$$

Noting that if $(\lambda + \gamma(\varphi - \varphi^{n-1}))^+ \neq 0$ then it holds

$$(\lambda + \gamma(\varphi - \varphi^{n-1}))^+ = \lambda + \gamma(\varphi - \varphi^{n-1}) \leq \lambda + \gamma\varphi$$

and thus it is

$$\min(\lambda + \gamma\varphi, (\lambda + \gamma(\varphi - \varphi^{n-1}))^+) = (\lambda + \gamma(\varphi - \varphi^{n-1}))^+.$$

Furthermore,

$$\lambda + \gamma\varphi \geq \lambda + \gamma(\varphi - \varphi^{n-1}) = (\lambda + \gamma(\varphi - \varphi^{n-1}))^+ \geq 0$$

and hence $\min(0, \lambda + \gamma\varphi) = 0$. In the other case, i.e., $(\lambda + \gamma(\varphi - \varphi^{n-1}))^+ = 0$ it holds

$$\min(\lambda + \gamma\varphi, (\lambda + \gamma(\varphi - \varphi^{n-1}))^+) = \min(0, \lambda + \gamma\varphi).$$

We conclude that we can rewrite $M_\gamma(\varphi, \lambda)$ as

$$\begin{aligned} M_\gamma(\varphi, \lambda) &= \frac{1}{2\gamma} \|\min(0, \lambda + \gamma\varphi) + (\lambda + \gamma(\varphi - \varphi^{n-1}))^+\|^2 - \frac{1}{2\gamma} \|\lambda\|^2 \\ &= \frac{1}{2\gamma} \|\min(0, \lambda + \gamma\varphi)\|^2 + \frac{1}{2\gamma} \|(\lambda + \gamma(\varphi - \varphi^{n-1}))^+\|^2 - \frac{1}{2\gamma} \|\lambda\|^2. \end{aligned}$$

Its Frechét derivative with respect to φ is given by

$$M'_\gamma(\varphi, \lambda) = \min(0, \lambda + \gamma\varphi) + (\lambda + \gamma(\varphi - \varphi^{n-1}))^+.$$

Using these calculations, we introduce the augmented Lagrangian

$$L_\gamma(\eta, \varphi, \lambda) = E_\epsilon(\eta, \varphi) + M_\gamma(\varphi, \lambda),$$

and the corresponding method reads as follows:

Algorithm 1. Augmented Lagrangian algorithm for the solution of (5)

Choose $\lambda_0 \in L^2(\Omega)$, $\gamma > 0$, and let $k = 0$.

repeat

Find $(\eta_{k+1}, \varphi_{k+1})$ solving

$$\min_{\eta, \varphi} L_\gamma(\eta, \varphi, \lambda_k)$$

or equivalently

$$\min_{\eta, \varphi} E_\epsilon(\eta, \varphi) + \frac{1}{2\gamma} \|\min(0, \lambda + \gamma\varphi)\|^2 + \frac{1}{2\gamma} \|(\lambda_k + \gamma(\varphi - \varphi^{n-1}))^+\|^2.$$

Update

$$\lambda_{k+1} = M'_\gamma(\varphi_{k+1}, \lambda_k)$$

$$k \leftarrow k + 1$$

until Stopping criterion (8) is satisfied

$$(\eta^n, \varphi^n) = (\eta_k, \varphi_k)$$

Remark 3.1. In our calculations, a natural choice for the initial guess λ_0 is given by λ^{n-1} from the previous time step. Such a type of initialization of the Lagrange multiplier has been used before by other authors in the context of parameterized families of constrained optimization problems. A recent example has been discussed in [27].

Applying [26, Theorem 4.45], for (η^n, φ^n) solving (5) it holds necessarily that there is some λ^n such that

$$\lambda^n = M'_\gamma(\varphi^n, \lambda^n), \quad (\eta^n, \varphi^n) = \operatorname{argmin}_{\eta, \varphi} E_\epsilon(\eta, \varphi) + M_\gamma(\varphi, \lambda^n).$$

Hence a reasonable stopping criterion for Algorithm 1 is given by

$$\max(\|\eta_{k-1} - \eta_k\|, \|\lambda_{k-1} - \lambda_k\|) \leq \text{TOL} \tag{8}$$

for some given tolerance $\text{TOL} > 0$.

4. Equations and finite element implementation

In this section, we derive from the energy functional (6) the corresponding Euler–Lagrange equations in variational form. These equations are the basis of our Galerkin finite element discretization. Finally, we describe our decoupled solution algorithm.

4.1. The Euler–Lagrange equations

In order to apply a Galerkin finite element method, we need to derive the Euler–Lagrange equations to the energy functional

$$\min_{\eta, \varphi} E_\epsilon(\eta, \varphi) + \frac{1}{2\gamma} \|(\lambda_k + \gamma(\varphi - \varphi^{n-1}))^+\|^2.$$

Differentiating with respect to η and φ , we obtain:

$$(((1 - \kappa)\varphi^2 + \kappa) \mathcal{G}\epsilon(\eta), e(w)) - (\tau, w)_{\partial_N \Omega} - (\alpha - 1)(\varphi^2 p_B, \operatorname{div} w) + (\varphi^2 \nabla p_B, w) = 0 \quad \forall w \in V, \quad (9)$$

as well as

$$(1 - \kappa)(\varphi \mathcal{G}\epsilon(\eta) : e(\eta), \psi) - 2(\alpha - 1)(\varphi p_B \operatorname{div} \eta, \psi) + 2(\varphi \nabla p_B \eta, \psi) + G_c \left(-\frac{1}{\varepsilon} (1 - \varphi, \psi) + \varepsilon(\nabla \varphi, \nabla \psi) \right) + ((\lambda + \gamma(\varphi - \varphi^{n-1}))^+, \psi) = 0 \quad \forall \psi \in W. \quad (10)$$

In order to solve both problems, we formulate a bilinear form for the linear elasticity part and a semi-linear form for the nonlinear phase-field as follows:

$$A_1(\eta, w) = (((1 - \kappa)\varphi^2 + \kappa) \mathcal{G}\epsilon(\eta), e(w)) - (\tau, w)_{\partial_N \Omega} - (\alpha - 1)(\varphi^2 p_B, \operatorname{div} w) + (\varphi^2 \nabla p_B, w) = 0 \quad \forall w \in V, \quad (11)$$

and

$$A_2(\varphi)(\psi) = (1 - \kappa)(\varphi \mathcal{G}\epsilon(\eta) : e(\eta), \psi) - 2(\alpha - 1)(\varphi p_B \operatorname{div} \eta, \psi) + 2(\varphi \nabla p_B \eta, \psi) + G_c \left(-\frac{1}{\varepsilon} (1 - \varphi, \psi) + \varepsilon(\nabla \varphi, \nabla \psi) \right) + ((\lambda + \gamma(\varphi - \varphi^{n-1}))^+, \psi) = 0 \quad \forall \psi \in W. \quad (12)$$

4.2. Galerkin finite element discretization

The computational domain is subdivided into quadrilateral or hexahedral element domains. Both subproblems are discretized using H^1 -conforming bilinear elements, i.e., the ansatz and test space uses Q_1^c -finite elements. Consequently, the discrete spaces have the property $V_h \subset V$ and $W_h \subset W$. The elasticity problem is linear and can be treated with an appropriate solver. Thus, for any given $\varphi^h \in W_h$ we can find $\eta^h \in V_h$ solving

$$A_1(\eta^h, w) = 0 \quad \forall w \in V_h.$$

Vice versa, for any given $\eta^h \in V_h$ we can solve the nonlinear problem of finding φ^h solving (12) with Newton's method. For the iteration steps $m = 0, 1, 2, \dots$, the Newton update is given by finding $\delta\varphi^h \in W_h$ solving:

$$\begin{aligned} A'_2(\varphi^{h,m})(\delta\varphi^h, \psi) &= -A_2(\varphi^{h,m})(\psi) \quad \forall \psi \in W_h, \\ \varphi^{h,m+1} &= \varphi^{h,m} + \omega \delta\varphi^h, \end{aligned} \quad (13)$$

with a line search parameter $\omega \in (0, 1]$. Here, we need the Jacobian of $A_2(\varphi)(\psi)$ applied to a direction $\delta\varphi$:

$$\begin{aligned} A'_2(\varphi)(\delta\varphi, \psi) &= (1 - \kappa)(\delta\varphi \mathcal{G}\epsilon(\eta) : e(\eta), \psi) - 2(\alpha - 1)(\delta\varphi p_B \operatorname{div} \eta, \psi) + 2(\delta\varphi \nabla p_B w, \psi) \\ &\quad + G_c \left(-\frac{1}{\varepsilon} (\delta\varphi, \psi) + \varepsilon(\nabla \delta\varphi, \nabla \psi) \right) + \gamma(\delta\varphi, \psi)_{\mathcal{A}(\varphi)} \end{aligned} \quad (14)$$

where

$$\mathcal{A}(\varphi) = \{x \in (0, L)^3 \mid \lambda + \gamma(\varphi - \varphi^{n-1}) > 0\}.$$

Summarizing, we deal with:

Problem 4.1 (Variational FE formulation for linear elasticity). Find $\eta^h \in V_h$ such that

$$A_1(\eta^h, w) = 0, \quad \forall w \in V_h,$$

and

Problem 4.2 (Variational FE formulation for phase-field). Find $\varphi^h \in W_h$ such that

$$A'_2(\varphi^{h,m})(\delta\varphi^h, \psi) = -A_2(\varphi^{h,m})(\psi), \quad \varphi^{h,m+1} = \varphi^{h,m} + \omega\delta\varphi^h, \quad (15)$$

for all $\delta\varphi^h \in W_h$ and where A_2 and A'_2 are given by (12) and (14).

4.3. The solution algorithm

Following [11], we use the quasi-static splitting approach as solution algorithm. Here, both systems are solved subsequently in an iterative way. This allows for easy extension for the usage of specific solvers for each of the subproblems. Our strategy is as follows: at time step t^n , for the given iteration φ^{l-1} , we solve first for η^l and then for the new φ^l with given η^l . Thus,

Problem 4.3 (Iteration of the decoupled problem). Let $\varphi^{h,l-1}$ be given from the previous iteration step. Find $\eta^{h,l} \in V_h$ such that

$$A_1(\eta^{h,l}, w) = 0, \quad \forall w \in V_h.$$

Take $\eta^{h,l}$ and solve for $\varphi^{h,l}$:

$$A'_2(\varphi^{h,m,l})(\delta\varphi^h, \psi) = -A_2(\varphi^{h,m,l})(\psi), \quad \varphi^{h,m+1,l} = \varphi^{h,m,l} + \omega\delta\varphi^h, \quad (16)$$

for all $\delta\varphi^h \in W_h$ and where A_2 and A'_2 are given by (12) and (14). The iteration is stopped when

$$\max(\|\eta_{l-1} - \eta_l\|, \|\varphi_{l-1} - \varphi_l\|) \leq \text{TOL}_2 \quad (17)$$

for some positive tolerance TOL_2 .

For the sake of simplicity, we use direct solvers to solve the linear sub-problems. However, the implementation of an iterative solver is straightforward.

The solution process is outlined in Algorithm 2.

Algorithm 2. Solution algorithm

For each time t^n

repeat

Solve augmented Lagrangian loop

repeat

Solve two-field problem iteratively, namely

Solve the linear elasticity using Problem 4.1

Solve the nonlinear phase-field using Problem 4.2.

until Stopping criterion (17) for two-field iteration is satisfied

Update

$$\lambda_{k+1} = (\lambda_k + \gamma(\varphi_{k+1} - \varphi^{n-1}))^+$$

until Stopping criterion (8) for augmented Lagrangian is satisfied

Set: $(\eta^n, \varphi^n) := (\eta_k, \varphi_k)$.

Increment $t^n \rightarrow t^{n+1}$.

Remark 4.4 (Parameter relation). A crucial aspect in phase-field is the choice of the parameters κ and ε in relation to the discretization parameter h . From the Γ -convergence we know that $\kappa \ll \varepsilon$. Although numerical analysis to our problem has not yet been demonstrated in the literature, we are aware of a related study [28], that $h \ll \kappa \ll \varepsilon$. Specifically, $h = o(\kappa)$ and $h = o(\varepsilon)$ should be chosen.

5. Numerical tests

We perform four numerical tests to investigate the augmented Lagrangian method. First, we solve Sneddon's 2d benchmark problem [29] (Chapter 2.4) with a constant pressure, which has been used in the literature for code validation [18,19,11]. In the second example, we consider a propagating crack, which is driven by an increasing pressure [11]. As third test case, two cracks are joining due to an increasing pressure. In fact, this example shows one of the advantages of the phase-field approach compared to other methods. In the final example, we compute Sneddon's 3d constant-pressure penny-shape crack [29] (Chapter 3.3). It is well-known that the phase-field approach needs fine meshes to work with sufficient accuracy. Thus, the aim of the study is to validate the proposed model by computing solutions on a hierarchy of locally

refined meshes in which a priori knowledge of crack propagation is taken into account. However, a simple automated refinement technique would be to use the mushy-zone of the phase-field function to mark cells for refinement for the next time step. In fact, such an approach for mesh refinement using an initial-point-set function (which has the same purpose as a phase-field function) is used in [30]. To the best of our knowledge, detailed numerical verification for pressurized cracks using a phase-field approach has not yet been performed for the test cases 5.2, 5.3, 5.4. All examples are computed with the multiphysics template [31], based on the finite element software deal.II [32].

5.1. Sneddon's 2D benchmark with constant pressure

The first example is motivated by Bourdin et al. [18] and is based on the theoretical calculations of Sneddon and Lowengrub [29] and Sneddon [33]. Specifically, we consider a 2D problem where a (constant) pressure p_B is used to drive the deformation and crack propagation. We assume a dimensionless form of the equations. The configuration is displayed in Fig. 7. Therefore, we deal with the following geometric data: $\Omega = (0, 4)^2$ and a (prescribed) initial crack with length $l_0 = 0.4$ on $\Omega_C = (1.8, 2.2) \times (2 - h, 2 + h) \subset \Omega$. As boundary conditions, we set the displacements zero on $\partial\Omega$. The initial penalization is given by $\gamma = 10^4$. The tolerance for the augmented Lagrangian method is $TOL = 10^{-4}$. We use a loosely-coupled scheme in which we solve only once per subproblem and then proceed to the next time step. The time step loop is run until the tolerance is $TOL = 10^{-5}$ is reached, i.e., $\|\eta^{n-1} - \eta^n\| \leq 10^{-5}$.

The Biot coefficient is $\alpha = 0$. The fracture toughness is chosen as $G_c = 1.0$. The mechanical parameters are Young's modulus and Poisson's ratio $E = 1.0$ and $\nu_s = 0.2$. The relationship to the Lamé coefficients μ_s and λ_s is given by:

$$\mu_s = \frac{E}{2(1 + \nu_s)}, \quad \lambda_s = \frac{\nu_s E_s}{(1 + \nu_s)(1 - 2\nu_s)}.$$

The injected pressure is $p_B = 10^{-3}$. Several parameters and geometry-related issues depend on the spatial mesh size parameter h . Namely, we provide a deeper understanding of their relation sketched in Remark 4.4 by undertaking four different tests:

- Case 1: Fix ε and κ ; refine h ,
- Case 2: Fix ε ; refine κ and h with $\kappa = h$,
- Case 3: Choose $\kappa = h$, $\varepsilon = 2h$; and then refine h ,
- Case 4: Choose $\kappa = 0.25\sqrt{h}$ and $\varepsilon = 0.5\sqrt{\kappa}$; and then refine h .

The final choice indeed reflects $h = o(\kappa)$ and $\kappa = o(\varepsilon)$. In addition, the initial (lower-dimensional) crack-line is extended by h in normal direction to approximate it as a volume as displayed in Fig. 3. Finally, the evaluation points of the normal displacements are placed depending on h as well, shown in Fig. 3, too.

Specifically, to compute the width w (or crack opening displacement, abbrev. COD), we have two different formulas:

- The jump of the normal displacements:

$$w = COD = [\eta(x, y) \cdot n(x, y)], \quad (18)$$

with evaluation at the points as displayed in Fig. 3.

- Integration in normal direction, such that

$$w = COD = \int_0^4 \eta(x_0, y) \cdot \nabla \varphi(x_0, y) dy, \quad (19)$$

where φ is as before our phase-field function and x_0 the x -coordinate of the integration line.

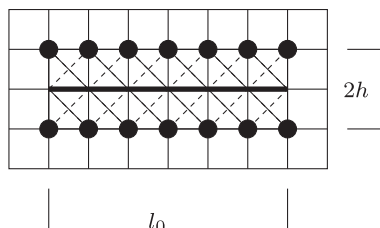


Fig. 3. Zoom-into the center of the domain Ω . The lower-dimensional crack with length $l_0 = 0.4$ (here a line in fat black) is approximated as a volume by extending it with mesh size h in normal up- and down-directions. The evaluation points for the normal displacements (to compute the crack opening displacement COD) using Formula (18) are displayed as dark circles. The volume extension of the crack and the evaluation points depend therefore both on the choice of h .

The goals of our studies are summarized as follows:

- Measuring the COD for different h and comparison to Sneddon's analytical results [29];
- Comparison of different parameter relations of h, κ, ε (Cases 1–4);
- Comparison of both COD evaluation formulas (18) and (19) for the last two (most relevant) cases;
- Comparison of the number of augmented Lagrangian iterations for each time step with respect to different h .

Our results might also be compared to [29,18,19,11]. The crack pattern and the corresponding mesh are displayed in Fig. 7. In the Figs. 4–6 the COD is shown. The solutions on the finest meshes of the Cases 1 and 2 (Fig. 4), do not show good convergence behavior, as it has to be expected. The mathematical more relevant Cases 3 and 4 fit well (away from the crack tips) with the analytical solution provided by Sneddon. Moreover, we observe that both evaluation formulas give the same limit for decreasing h . As seen in Table 1, for the chosen tolerance 10^{-5} for the time step loop, we have a very good approximation after only one time step. This is in agreement with our expectations because the setting of this test is fully stationary.

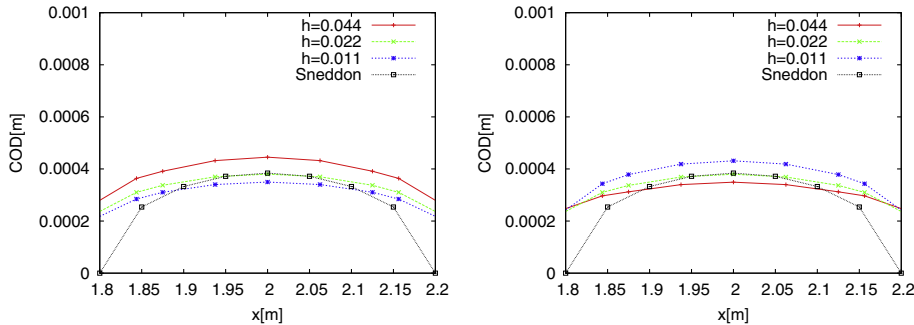


Fig. 4. Example 1, Cases 1 and 2: COD for different h . In the plot, we have $h := h_{\min}$. Sneddon's black line corresponds to his analytical solution. On the left, the COD is computed with formula (18) and on the right with formula (19). Both formulas show good agreement in computing the COD.

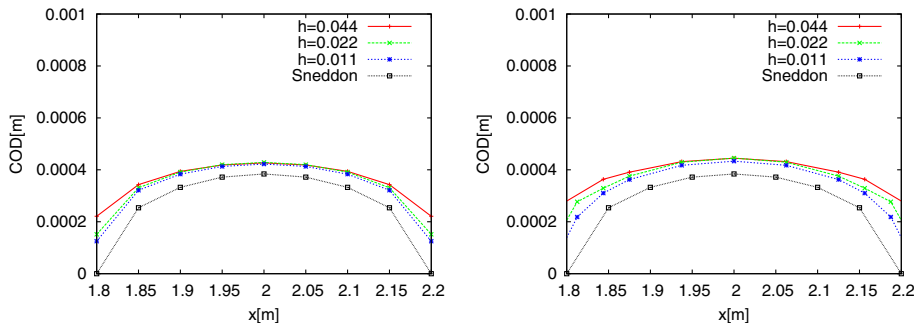


Fig. 5. Example 1, Case 3: COD for different h . In the plot, we have $h := h_{\min}$. Sneddon's black line corresponds to his analytical solution. On the left, the COD is computed with formula (18) and on the right with formula (19). Both formulas show good agreement in computing the COD.

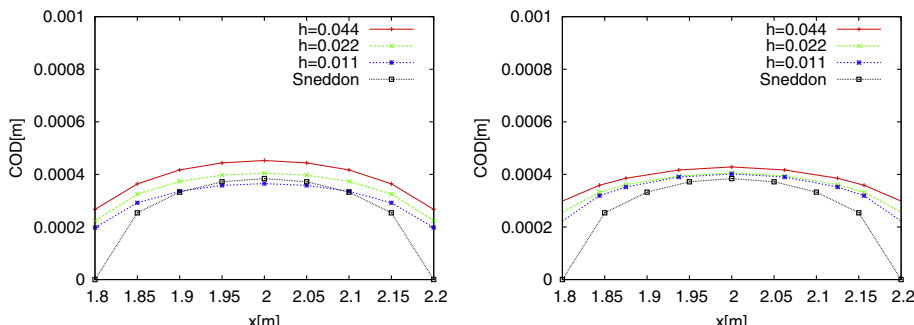


Fig. 6. Example 1, Case 4: COD for different h . In the plot, we have $h := h_{\min}$. Sneddon's black line corresponds to his analytical solution. On the left, the COD is computed with formula (18) and on the right with formula (19). Both formulas show good agreement in computing the COD.

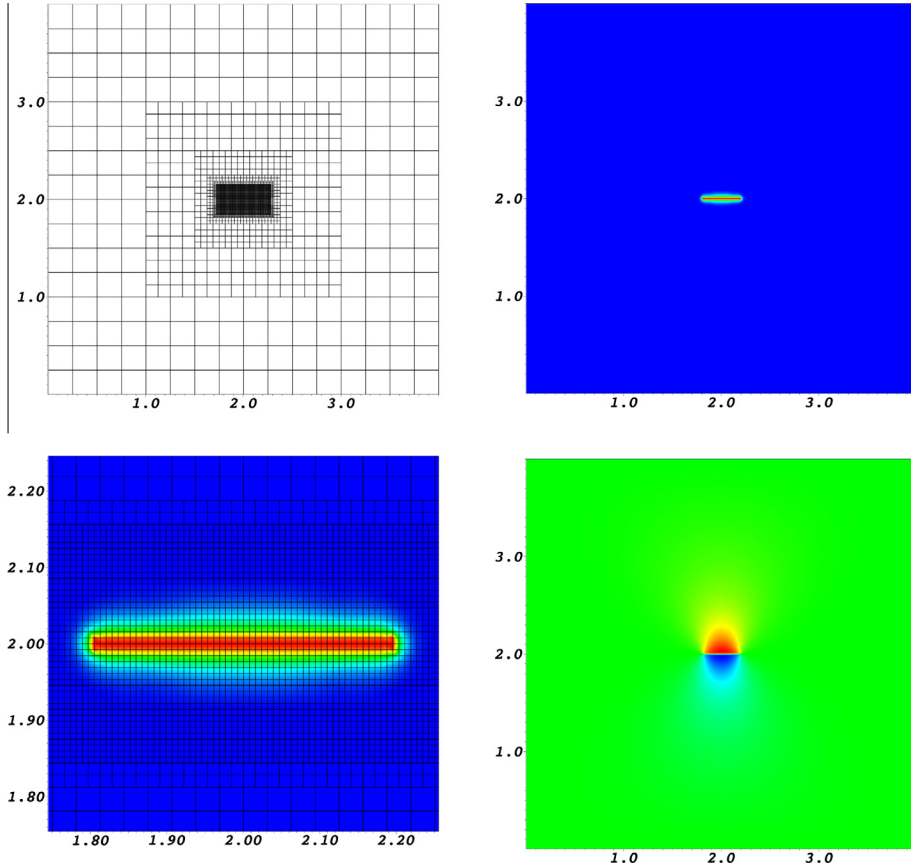


Fig. 7. Example 1: mesh and geometry, location of crack, zoom-in of the mesh with the crack pattern, and finally, normal displacements (required to compute the COD of the crack) are displayed from top left to bottom right. The green part in the third subfigure shows the thickness ε of the mushy-zone in the phase-field variable. (For interpretation of the references to colour in this figure caption, the reader is referred to the web version of this article.)

Table 1

Comparison of λ -iterations for each time step with respect to h for all four cases going from left to right.

Timestep	h_{\min}	λ -iter	λ -iter	λ -iter	λ -iter
0	0.044	16	13	13	13
1	0.044	7	7	7	8
0	0.022	16	16	12	17
1	0.022	13	13	10	13
0	0.011	23	23	17	22
1	0.011	24	24	12	23

In all tests the time step tolerance is already reached in the second iteration. We also notice that in these two-dimensional test cases, good agreement of the functional values is already achieved on relative coarse meshes.

5.2. Increasing pressure leading to crack propagation

We keep the geometry, all parameters, and tolerances as in the first example. The only two changes compared to the previous example are:

- Using an increasing pressure,

$$p = k\bar{p}$$

with $\bar{p} = 0.1$,

- computing a fixed number of 23 time steps with time step size $k = 1$.

The goals in this study are

- to observe the total length of the crack with respect to spatial mesh refinement; distribution of the COD.

The mesh and the initial crack are displayed in Fig. 8. A sequence of crack patterns are provided in Fig. 9. In fact, until time step 19, we only observe almost no growth. Then, since G_c is exceeded, we have brutal crack growth as also observed by Bourdin et al. [6] and Miehe et al. [7] in the case of pure elasticity. A qualitative distribution of the COD is shown in

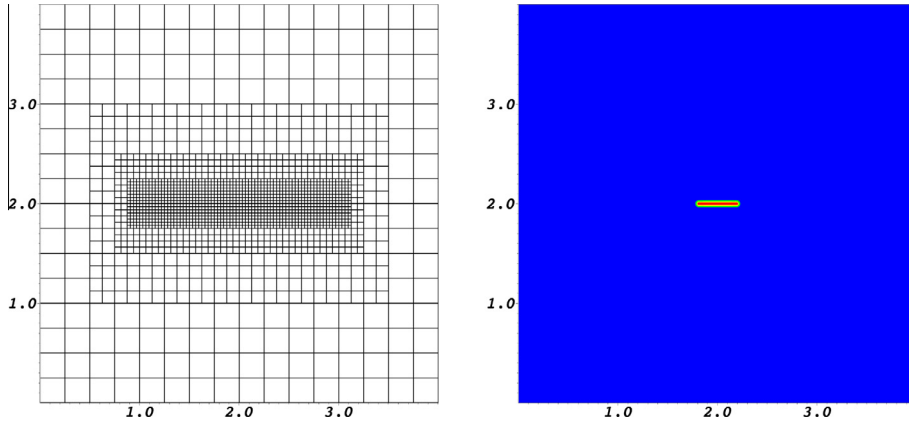


Fig. 8. Example 2: locally refined grid and initial crack pattern.

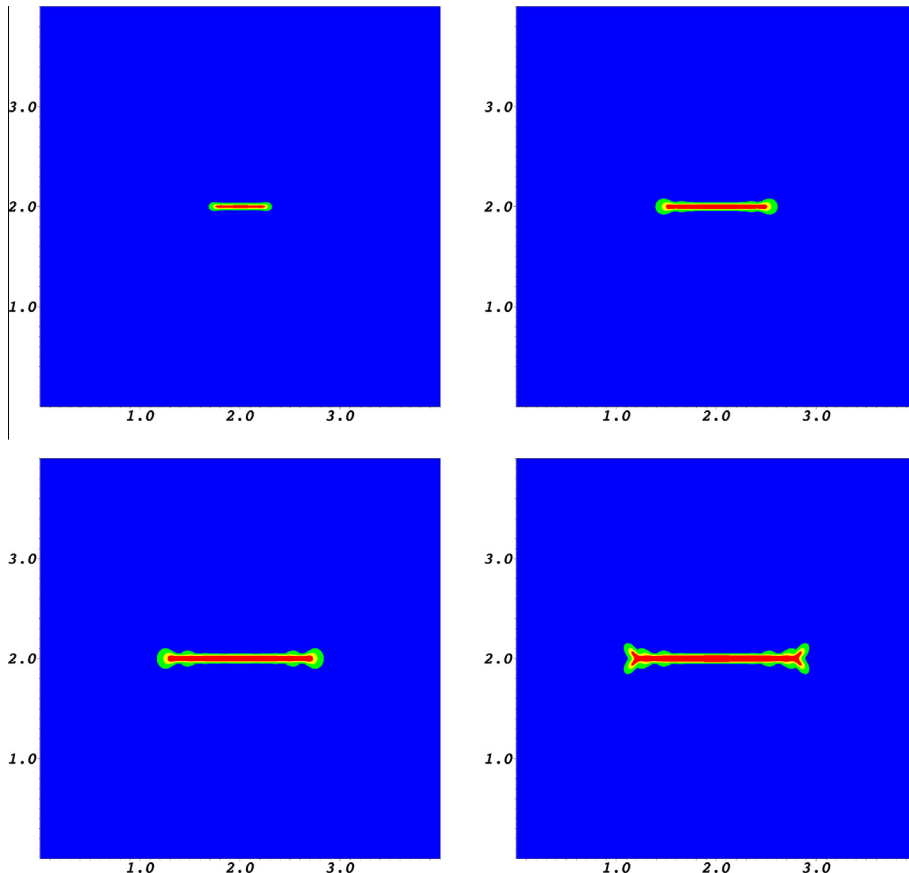


Fig. 9. Example 2: crack pattern for the last four time steps at $T = 20, 21, 22, 23$.

Fig. 10. Here, we notice that the COD has its largest value in the center of the crack and becomes smaller towards both tips. This is physically reasonable and a good criterion for validation. Finally, we compare the total crack length on three different meshes in Fig. 11.

5.3. Increasing pressure leading to joining cracks

The third example demonstrates a major capability of the phase-field approach: joining of two cracks without using any special geometry-adapted technique. We keep all parameters as in the previous example. The first crack (named as crack 1) is the same as before and centered in the middle of the domain. The second crack (named as crack 2) is vertically-oriented at $x = 2.6$ and $1.8 \leq y \leq 2.2$ and is also extended by h in normal (x_-) direction. Consequently, the shortest distance of the two cracks is 0.4. As in the previous example, we compute 23 time steps with time step size $k = 1$. While applying an increasing pressure,

$$p = k\bar{p},$$

with $\bar{p} = 0.1$, we are able to study the propagation of both cracks and their joining. The goal is again to perform studies for different h and to detect the time when both cracks meet. Therefore, we observe the distance between the cracks. In addition, we perform a set of computations on a 10% distorted mesh. This is a good test, to see if the crack path is independent of the mesh structure (which of course should be the case!). The meshes are displayed in Fig. 12.

Observing the results provides us with the following understanding. In Fig. 13, the four final crack patterns on the finest mesh are displayed. Before time step 20 almost no crack growth is observed. Then, brutal crack growth as in the previous example occurs. The final crack pattern to both meshes are shown in Fig. 14. Indeed, the pattern is independent of the mesh-structure which is a very important observation. Quantitative findings to the brutal growth and the joining are provided for different meshes in Fig. 15.

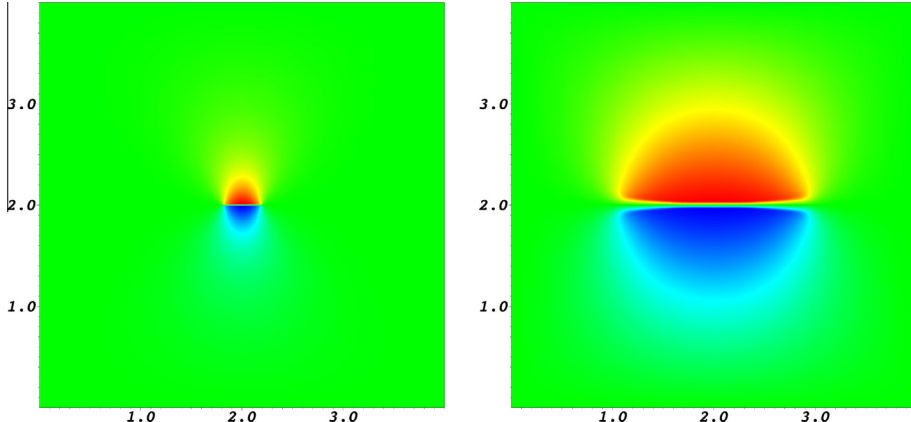


Fig. 10. Example 2: normal displacement (for the computation of the width) at the beginning and final times $T = 1, 23$. It is very important to notice that the color scheme and its density indicate that the COD has its largest value in the center of the crack and becomes smaller towards both tips. This is physically reasonable and a good criterion for validation.

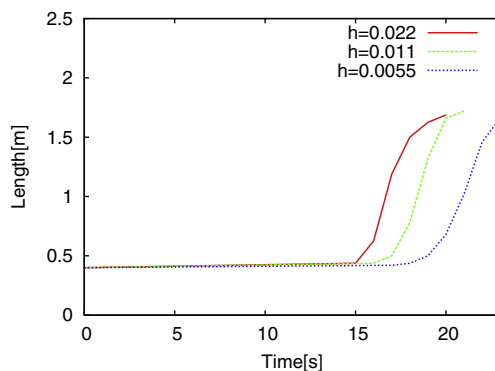


Fig. 11. Example 2: total crack length versus time on three mesh levels. In the plot, we have $h := h_{\min}$. The crack starts growing between time step 15 and 20 depending on the refinement level.

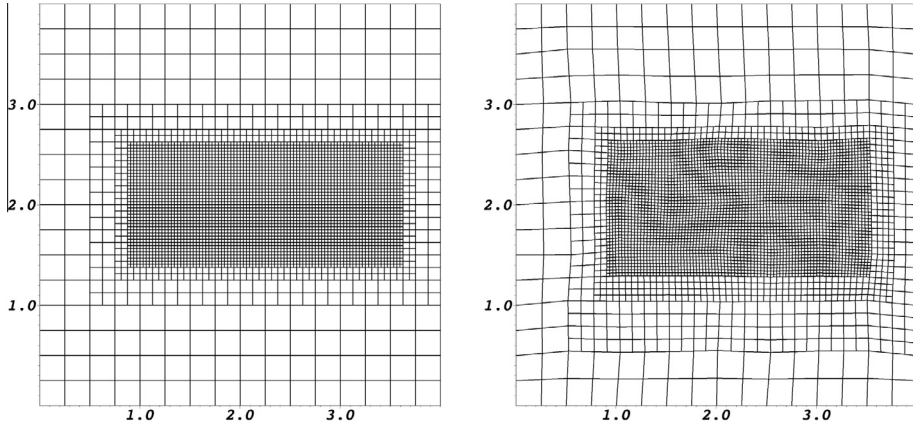


Fig. 12. Example 3: meshes for both sets of computations: locally refined mesh (left) and the same mesh but randomly distorted (right).

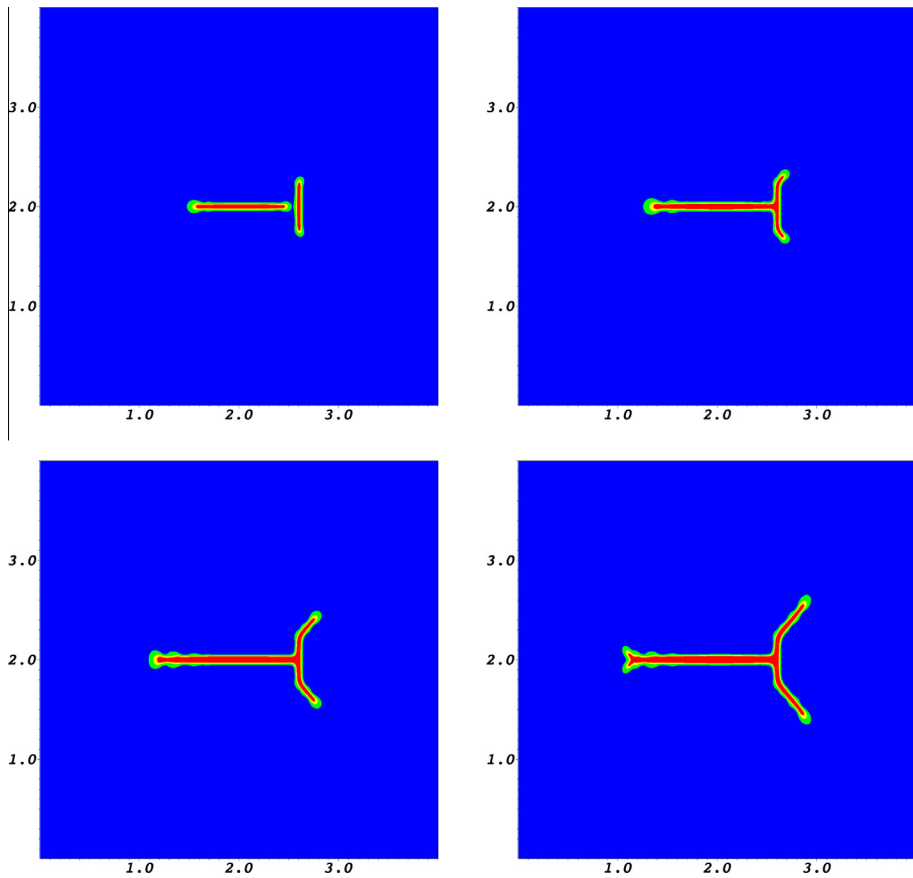


Fig. 13. Example 3: crack pattern for the last four time steps at $T = 20, 21, 22, 23$.

5.4. Sneddon's 3d benchmark with constant pressure

In the final example, we upgrade our code to three dimensions. In the cube $\Omega = (0, 10)^3$, we prescribe a penny-shape crack with radius $r = 1.0$ in the $y = 5.0$ -plane with mid-point $(5.0, 5.0, 5.0)$ and which is subject to a constant pressure $p_B = 10^{-3}$. The configuration and the initial crack are displayed in Fig. 16 at top left. As boundary conditions we set the displacements zero on $\partial\Omega$. The material parameters (i.e., G_c, E , etc.) are the same as in the 2D examples. The initial penalization parameter is

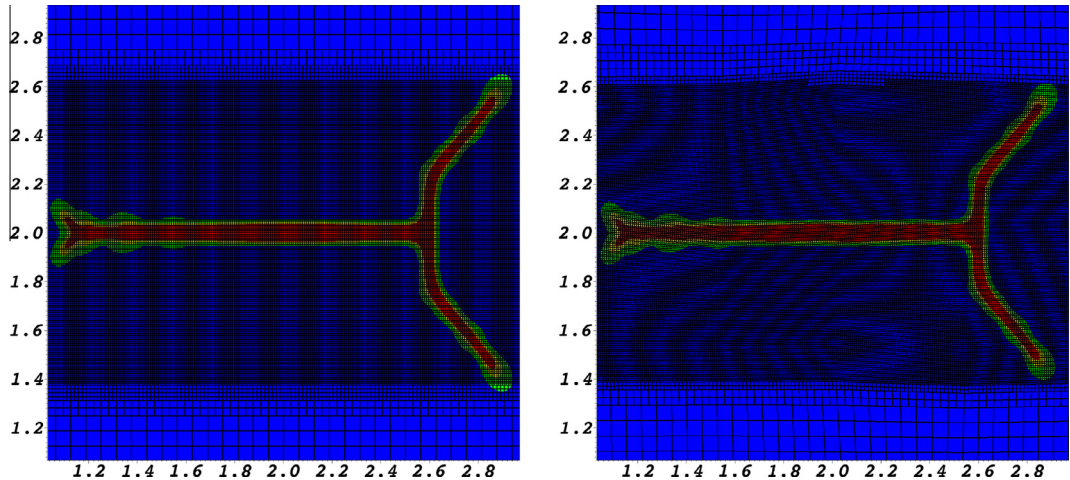


Fig. 14. Example 3: crack patterns for final time steps on the two different meshes with the distorted mesh on the right side. Comparing the graphical solutions, we observe that the crack pattern and propagation is independent of the mesh.

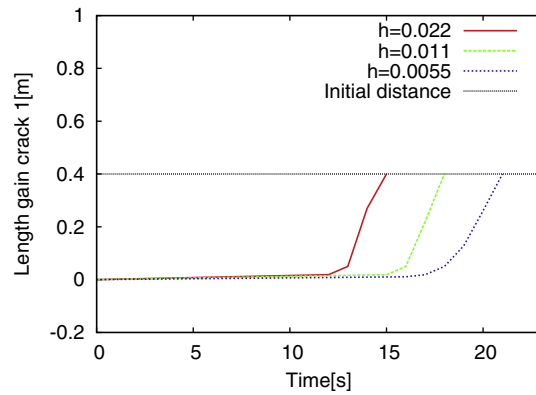


Fig. 15. Example 3: length gain of crack 1 into east direction. Both cracks join (at latest) when crack 1 reaches the center of crack 2. The initial distance between both cracks is 0.4.

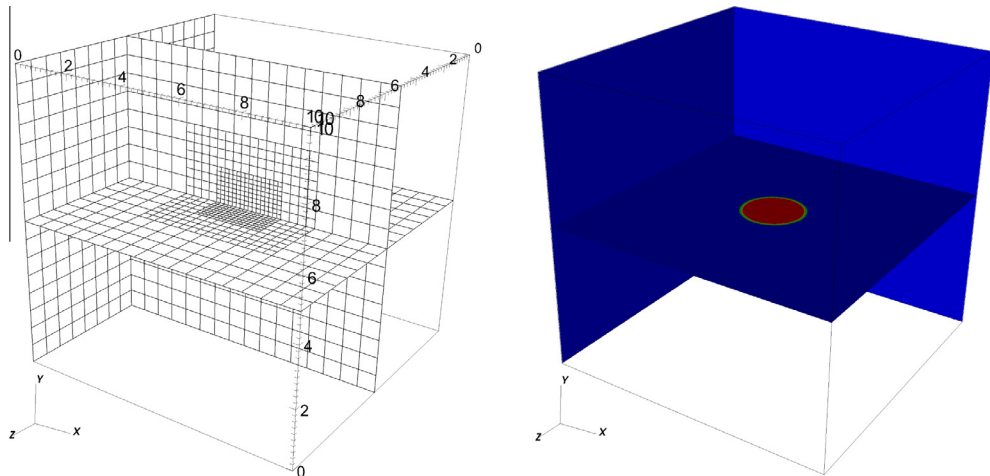


Fig. 16. Example 4: geometry information with locally refined grid and location of the penny-shape crack.

given by $\gamma = 10^2$. The tolerances are the same as in the 2D cases. The setup is again motivated by [29] (Chapter 3.3) who also provides an analytical expression to compute the normal displacements (from which we obtain the COD):

$$u_y(r, y_m) = \frac{2(1-r)p_p}{\pi} \sqrt{1 - (r-5)^2},$$

where $4 \leq r \leq 6$ (such that the radius of the penny-shape crack is ≤ 1) and $y_m = (5.0, 5.0, 5.0)$ denotes the origin of the penny-shape fracture. The results of the normal displacements are provided in Fig. 17.

The goal of this test is twofold:

- Compare to Sneddon's analytical solution,
- Perform computations on different spatial mesh levels.

The evaluation of the COD is only performed with formula (18) because it has been shown in the 2D test that they deliver the same results.

Analyzing our computations, we first notice that the time step tolerance is reached in 3 iterations (instead of 2 in the two-dimensional case). Our results show convergence with respect to spatial mesh refinement as illustrated in Fig. 18. Moreover, the values converge towards the analytical solution. From both findings, we infer that our model works correctly. Finally, we aim to give a better understanding of our results and show several zoomed findings in Fig. 19. In the top left of Fig. 19, we observe the location of the crack in the refined mesh. Of course, since we are only interested in the COD and no propagation, we adapted the local mesh refinement to the initial location of the crack. This could easily be adapted for propagating cracks as done in the 2D test cases or dynamically as described in the introduction to all four test cases. Specifically, we point out the volume approximation of the crack related to ε (and h) is shown in the top right and bottom left of Fig. 19. In the bottom right of Fig. 19, we emphasize that the largest crack opening is in the center of the crack and decreases towards the ends.

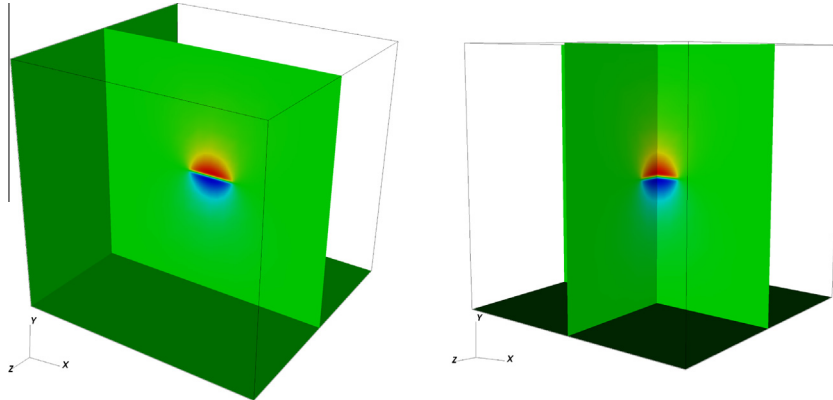


Fig. 17. Example 4: normal displacements for determining the COD.

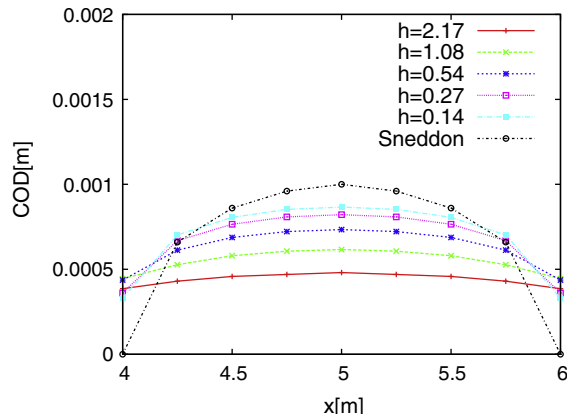


Fig. 18. Example 4: COD for different h . Sneddon's black line corresponds to his analytical 3D solution.

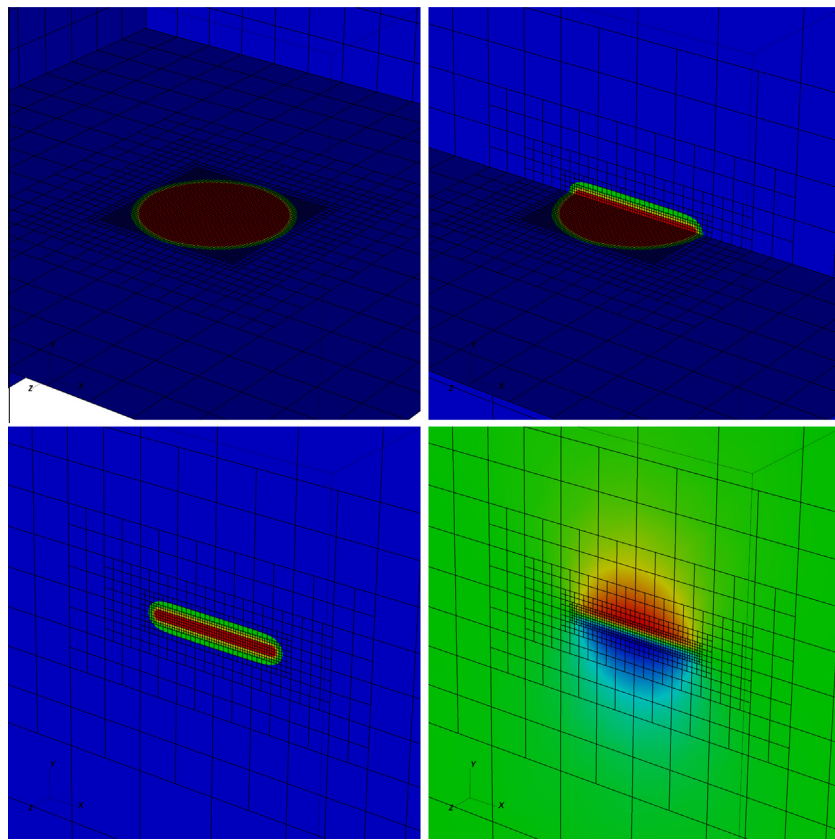


Fig. 19. Example 4: zoom-in in which the location (top left) and the volume approximation by extending in normal up- and down direction are illustrated (2nd and 3rd figure). Finally, a zoom-into show the normal displacements is provided, which also shows that the largest crack opening is in the center of the crack and decreases towards the end (see also Fig. 18).

6. Conclusions

In this work, we considered a phase-field formulation to treat pressurized fractures. In order to force the irreversibility of crack growth, a time inequality constraint is required, which is realized as a penalization. A robust method is based on the augmented Lagrangian approach which is substantiated with several numerical tests, namely pressurized propagating fractures, which are (still) very challenging to solve. Since detailed numerical studies are missing in the literature, we investigated simple, but challenging, configurations. As future extension, we plan to consider three-dimensional propagating penny-shape fractures.

Acknowledgments

The third author thanks the Center for Subsurface Modeling at ICES, UT Austin, for hosting his research stay in July 2013 and the DAAD (German Academic Exchange Service) for a travel grant vital to the initialization of this collaboration. The second author is grateful to the Alexander von Humboldt foundation supporting since October 2013 other studies build upon the present work.

References

- [1] A. Griffith, The phenomena of rupture and flow in solids, *Philos. Trans. R. Soc. London* 221 (1921) 163–198.
- [2] N. Moes, J. Dolbow, T. Belytschko, A finite element method for crack growth without remeshing, *Int. J. Numer. Methods Eng.* 46 (1999) 131–150.
- [3] I. Babuska, J. Belenk, The partition of unity method, *Int. J. Numer. Methods Eng.* 40 (1997) 727–758.
- [4] G. Francfort, J.-J. Marigo, Revisiting brittle fracture as an energy minimization problem, *J. Mech. Phys. Solids* 46 (1998) 1319–1342.
- [5] B. Bourdin, G. Francfort, J.-J. Marigo, Numerical experiments in revisited brittle fracture, *J. Mech. Phys. Solids* 48 (2000) 797–826.
- [6] B. Bourdin, G. Francfort, J.-J. Marigo, The variational approach to fracture, *J. Elast.* 91 (2008) 1–148.
- [7] C. Miehe, F. Welschinger, M. Hofacker, Thermodynamically consistent phase-field models of fracture: variational principles and multi-field finite element implementations, *Int. J. Numer. Methods Eng.* 83 (2013) 1273–1311.
- [8] C. Miehe, M. Hofacker, F. Welschinger, A phase field model for rate-independent crack propagation: robust algorithmic implementation based on operator splits, *Comput. Methods Appl. Mech. Eng.* 199 (2010) 2765–2778.

- [9] M.J. Borden, C.V. Verhoosel, M.A. Scott, T.J.R. Hughes, C.M. Landis, A phase-field description of dynamic brittle fracture, *Comput. Methods Appl. Mech. Eng.* 217 (2012) 77–95.
- [10] M. Hofacker, C. Miehe, Continuum phase field modeling of dynamic fracture: variational principles and staggered FE implementation, *Int. J. Fract.* 178 (2012) 113–129.
- [11] A. Mikelić, M. Wheeler, T. Wick, A quasi-static phase-field approach to the fluid filled fracture, 2013, ICES Report 13–22.
- [12] B. Lecampion, E. Detournay, An implicit algorithm for the propagation of hydraulic fracture with a fluid lag, *Comput. Methods Appl. Mech. Eng.* 196 (2007) 4863–4880.
- [13] B.A. Schrefler, S. Secchi, L. Simoni, On adaptive refinement techniques in multi-field problems including cohesive fracture, *Comput. Methods Appl. Mech. Eng.* 195 (2006) 444–461.
- [14] B. Carrier, S. Granet, Numerical modeling of hydraulic fracture problem in permeable medium using cohesive zone model, *Eng. Fract. Mech.* 79 (2012) 312–328.
- [15] F. Iralz, J.J. Remmers, J.M. Huyghe, R. de Borst, A large deformation formulation for fluid flow in a progressively fracturing porous material, *Comput. Methods Appl. Mech. Eng.* 256 (2013) 29–37.
- [16] B. Ganis, M. Mear, A. Sakhaei-Pour, M. F. Wheeler, T. Wick, Modeling fluid injection in fractures with a reservoir simulator coupled to a boundary element method, *Computational Geosciences*, accepted for publication, <http://dx.doi.org/10.1007/s10596-013-9396-5>.
- [17] S. Castonguay, M. Mear, R. Dean, J. Schmidt, Predictions of the growth of multiple interacting hydraulic fractures in three dimensions, SPE-166259-MS (2013) 1–12.
- [18] B. Bourdin, C. Chukwudzie, K. Yoshioka, A variational approach to the numerical simulation of hydraulic fracturing, *SPE Journal, Conference Paper 159154-MS* (2012).
- [19] A. Mikelić, M. Wheeler, T. Wick, A phase-field approach to the fluid filled fracture surrounded by a poroelastic medium, 2013, ICES Report 13–15.
- [20] F.A. Lootsma, Hessian matrices of penalty functions for solving constrained-optimization problems, *Philips Res. Rep.* 24 (1969) 322–330.
- [21] W. Murray, Analytical expressions for the eigenvalues and eigenvectors of the Hessian matrices of barrier and penalty functions, *J. Optim. Theory Appl.* 7 (1971) 189–196.
- [22] M.R. Hestenes, Multiplier and gradient methods, *J. Optim. Theory Appl.* 4 (1969) 303–320.
- [23] M.J.D. Powell, A method for nonlinear constraints in minimization problems, in: *Optimization (Sympos., Univ. Keele, Keele, 1968)*, Academic Press, 1969, pp. 283–298.
- [24] M. Fortin, R. Glowinski, Augmented Lagrangian methods: applications to the numerical solution of boundary value problems, *Stud. Math. Appl.* 15 (1983).
- [25] R. Glowinski, P.L. Tallec, Augmented Lagrangian and operator-splitting methods in nonlinear mechanics, *SIAM Stud. Appl. Math.* 9 (1989).
- [26] K. Ito, K. Kunisch, *Lagrange multiplier approach to variational problems and applications, Advances in Design and Control*, vol. 15, Society for Industrial and Applied Mathematics (SIAM), Philadelphia, PA, 2008.
- [27] R. Glowinski, A. Quaini, On an inequality of C. Sundberg: a computational investigation via nonlinear programming, *J. Optim. Theory Appl.* 158 (2013) 739–772.
- [28] B. Bourdin, Image segmentation with a finite element method, *M2AN* 33 (1999) 229–244.
- [29] I.N. Sneddon, M. Lowengrub, *Crack problems in the classical theory of elasticity*, SIAM Series in Applied Mathematics, John Wiley and Sons, Philadelphia, 1969.
- [30] T. Wick, Flapping and contact fsi computations with the fluid-solid interface-tracking/interface-capturing technique and mesh adaptivity, *Comput. Mech.* (2013).
- [31] T. Wick, Solving monolithic fluid-structure interaction problems in arbitrary Lagrangian Eulerian coordinates with the deal.ii library, *Arch. Numer. Softw.* 1 (2013) 1–19.
- [32] W. Bangerth, T. Heister, G. Kanschat, et al., Differential equations analysis library, 2012.
- [33] I.N. Sneddon, The distribution of stress in the neighbourhood of a crack in an elastic solid, *Proc. R. Soc. London A* 187 (1946) 229–260.